High-temperature rotational-vibrational O_2–CO_2 coherent Raman spectroscopy with ultrabroadband femtosecond laser excitation generated in-situ

Mazza, Francesco; Griffioen, Nathan; Castellanos, Leonardo; Kliukin, Dmitrii; Bohlin, Alexis

DOI
10.1016/j.combustflame.2021.111738

Publication date
2022

Document Version
Final published version

Published in
Combustion and Flame

Combustion and Flame 237 (2022) 111738

Contents lists available at ScienceDirect

Combustion and Flame

journal homepage: www.elsevier.com/locate/combustflame

High-temperature rotational-vibrational O_2-CO_2 coherent Raman spectroscopy with ultrabroadband femtosecond laser excitation generated *in-situ*

Francesco Mazza[a,*], Nathan Griffioen[a], Leonardo Castellanos[a], Dmitrii Kliukin[a], Alexis Bohlin[a,b]

[a] *Advanced Laser Diagnostics and Flames Laboratory, Aerodynamics, Wind Energy, Flight Performance & Propulsion (AWEP) Department, Delft University of Technology, Kluyverweg 1, 2629 HS Delft, the Netherlands*

[b] *Space Propulsion Laboratory, Department of Computer Science, Electrical and Space Engineering, Luleå University of Technology, Bengt Hultqvists väg 1, 981 92 Kiruna, Sweden*

ARTICLE INFO

Article history:
Received 6 March 2021
Revised 30 August 2021
Accepted 5 September 2021
Available online 24 September 2021

Keywords:
Laser diagnostics
Gas-phase thermometry
Lean premixed flames
Femtosecond/picosecond CARS

ABSTRACT

We present ultrabroadband two-beam femtosecond/picosecond coherent Raman spectroscopy on the ro-vibrational spectra of CO_2 and O_2, applied for multispecies thermometry and relative concentration measurements in a standard laminar premixed hydrocarbon flame. The experimental system employs fs-laser-induced filamentation to generate the compressed supercontinuum *in-situ*, resulting in a ~24 fs full-width-at-half-maximum pump/Stokes pulse with sufficient bandwidth to excite all the ro-vibrational Raman transitions up to 1600 cm^{-1}. We report the simultaneous recording of the ro-vibrational CO_2 Q-branch and the ro-vibrational O_2 O-, Q- and S-branch coherent Stokes Raman spectra (CSRS) on the basis of a single-laser-shot. The use of filamentation as the supercontinuum generation mechanism has the advantage of greatly simplifying the experimental setup, as it avoids the use of hollow-core fibres and chirped mirrors to deliver a near-transform-limited ultrabroadband pulse at the measurement location. Time-domain models for the ro-vibrational Q-branch spectrum of CO_2 and the ro-vibrational O-, Q- and S-branch spectra of O_2 were developed. The modelling of the CO_2 Q-branch spectrum accounts for up to 180 vibrational bands and for their interaction in Fermi polyads, and is based on recently available, comprehensive calculations of the vibrational transition dipole moments of the CO_2 molecule: the availability of spectroscopic data for these many vibrational bands is crucial to model the high-temperature spectra acquired in the flue gases of hydrocarbon flames, where the temperature can exceed 2000 K. The numerical code was employed to evaluate the CSRS spectra acquired in the products of a laminar premixed methane/air flame provided on a Bunsen burner, for varying equivalence ratio in the range 0.6–1.05. The performance of the CO_2 spectral model is assessed by extracting temperatures from 40-laser-shots averaged spectra, resulting in thermometry accuracy and precision of ~5% and ~1%, respectively, at temperatures as high as 2220 K.

1. Introduction

Coherent Raman scattering spectroscopy – both in its Stokes (CSRS) and anti-Stokes (CARS) implementation [1,2] – has found vast application in the experimental study of chemically-reacting flows, especially in the context of combustion [3] and non-equilibrium thermodynamics [4]. CARS in particular has been extensively employed in combustion diagnostics for temperature [5–7] and concentration measurements [8–10], and is regarded as the gold-standard for high-fidelity thermometry in flames [11–13]. In principle, CARS is a form of four-wave mixing (FWM) [14], i.e. a third-order non-linear optical process, in which the frequency difference of two photons –called the "pump" photon (with angular frequency ω_p) and the "Stokes" photon (ω_{St})– coherently excite a Raman-active molecule to a higher rotational-vibrational (ro-vibrational) energy state; a third photon, the "probe" (ω_{pr}), is then scattered by the molecule, resulting in the emission of a coherent CARS photon at frequency $\omega_{CARS} = \omega_p - \omega_{St} + \omega_{pr}$. In the CARS process, the pump/Stokes photon-pairs couple to the internal energy states of the Raman-active molecules: the CARS

* Corresponding author.
E-mail address: f.mazza@tudelft.nl (F. Mazza).

https://doi.org/10.1016/j.combustflame.2021.111738

signal thus carries information on the molecular distribution over the ro-vibrational energy manifold, usually described in terms of the vibrational and total-angular-momentum quantum numbers (v and J, respectively). In the context of ro-vibrational spectroscopy ($\Delta v=\pm 1$) it is customary to use the labels "Q-", "O-", and "S-branch" to indicate ro-vibrational transitions with $\Delta J=0$, -2, and $+2$, respectively [15].

The commercial availability, in recent years, of ultrafast regenerative amplifiers, has prompted the development of a number of time-resolved CARS techniques, allowing for nearly collision-independent measurements at high repetition rate [10]. In addition, the typical CARS setup can be greatly simplified when a broadband laser source is employed, as the constructive photon-pairs, typically provided by two distinct laser pulses, can be found across the bandwidth of a single pump/Stokes pulse. This technique is called "two-beam CARS" [11]. A single ultrafast regenerative amplifier, providing <50 fs duration pulses, can impulsively excite all the rotational energy states that are significantly populated by N_2 molecules at flame temperatures [16]. Nevertheless, the bandwidth of the laser pulses provided by commercially-available ultrafast regenerative amplifiers is not sufficient to efficiently excite Raman transitions further than ~400 cm^{-1}. In order to achieve impulsive excitation and perform ro-vibrational two-beam CARS spectroscopy in the "molecular fingerprint" region (i.e. in the range 800–1800 cm^{-1}) it is necessary to compress the pump/Stokes pulse to a duration comparable to the vibrational period of the target molecules [17], this being e.g. ~25 fs for CO_2 and ~21 fs for O_2. Thus, when compressing the pump/Stokes pulse below 25 fs duration, the resulting ultrabroadband pulse has enough spectral bandwidth to provide a significant number of constructive photon-pairs at Raman shifts up to ~1600 cm^{-1}. The use of ultrabroadband laser pulses to excite the whole ro-vibrational energy manifold of the Raman-active molecules in the probe volume dramatically enlarges the interrogation window for quantitative multiplex spectroscopy. Roy et al. [18] demonstrated the use of supercontinuum generation, through an argon-filled hollow-core fibre, in a single-beam CARS setup to measure the number density of CO_2 in a binary mixture with argon at room temperature and at different pressures. Bohlin and Kliewer [19] employed a hollow-core fibre to compress the 45 fs duration output of a Ti:Sapphire regenerative amplifier below 7 fs, enough to impulsively excite Raman transitions in the spectral range 0–4200 cm^{-1}. They demonstrated single-shot one-dimensional imaging of the ro-vibrational spectra of N_2, O_2, H_2, CO_2, and CH_4 in a two-beam femtosecond/picosecond (fs/ps) CARS setup. The application of this experimental technique to combustion diagnostics was furthermore demonstrated, firstly in a flat hydrocarbon flame [20] and subsequently in the investigation of flame-wall interaction [21]. Odhner et al. [22] demonstrated time-resolved ultrabroadband Raman spectroscopy employing fs-laser-induced air filamentation to generate the supercontinuum excitation pulse. They employed a 2 mJ, 45 fs duration laser pulse to generate a plasma filament in atmospheric air: the self-phase modulation experienced by the pulse resulted in its temporal compression to ~14 fs; furthermore, they showed the use of this "heterodyned, impulsive filament-based, stimulated Raman technique" in a CH_4/O_2 flame.

The diagnostic technique presented in this work relies on such filament-based supercontinuum generation to achieve quantitative time-resolved coherent Raman spectroscopy in the molecular fingerprint region. The possibility of performing measurements in the molecular fingerprint region is particularly appealing for combustion diagnostics, as almost all major combustion species possess ro-vibrational Raman spectral lines in this spectral range. The ro-vibrational Raman spectrum of O_2 is located at ~1556 cm^{-1} [23], while CO_2 appears a Fermi dyad at ~1285 cm^{-1} and ~1388 cm^{-1} [24], and the pure-rotational Raman spectrum of H_2 spans from ~354 cm^{-1} to ~1815 cm^{-1}, at high temperatures [25]. In addition, almost all hydrocarbons (e.g. methane, ethylene and ethane) have Raman-active vibrational transitions in the range ~882–1791 cm^{-1} [26], corresponding to the bending mode of the H–C-H bond. The scope of the present work is limited to the development of ultrabroadband two-beam fs/ps coherent Raman spectroscopy for the measurement of the ro-vibrational CO_2 and O_2 spectra in the region 1200–1600 cm^{-1}. The simultaneous detection of these two main combustion species makes the technique appealing for the study of Moderate or Intense Low oxygen Dilution (MILD) combustion [27–29] applications, where hot flue gases are recirculated as a thermal control mechanism to abate the emission of nitric oxide, leading to O_2 dilution and relatively low temperatures. Moreover, the availability of both O_2 and CO_2 as thermometric species in this spectral region makes the technique suited to applications such as oxy-fuel combustion, where molecular nitrogen is not available as a thermometer [30]. Multiplex CARS spectroscopy on the CO_2 Q-branch spectrum has been an active research area since the first applications of CARS to gas-phase media. In 1984, Hall and Stufflebeam [31] reported on CO_2 CARS thermometry performed at temperatures up to ~1600 K in a gas cell. A dual-pump nanosecond CARS system was employed by Lucht et al. [32] to simultaneously detect the Q-branch spectra of CO_2 and N_2 (at ~2330 cm^{-1}): they measured temperatures up to ~2000 K and achieved single-shot detection of the CO_2 signal at values of the mole fraction down to ~1–2%. Dual-pump N_2-CO_2 CARS was furthermore used for thermometry and CO_2 concentration measurements in the exhaust of a swirl-stabilized JP-8-fuelled combustor [33]. Recently, Kerstan et al. [34] demonstrated the first use of ultrabroadband two-beam fs/ps CARS for CO_2 thermometry. They used a neon-filled hollow-core fibre to compress the ~35 fs duration laser pulse, resulting in a ~7 fs duration, ~25 μJ pump/Stokes pulse. Due to the relatively low average power of the laser pulses employed, their measurements were limited to a pressurized gas-cell and the maximum temperature measured from the CO_2 spectrum was 937 K. The same research group demonstrated the use of ultrabroadband CARS –attained in this case through an optical parametric chirped-pulse amplifier, providing a ~7 fs duration, 7.5 μJ pump/Stokes pulse– to measure relative CO/CO_2 concentrations, as well as temperature, in a gas oven heated up to ~800 K [35].

In the present work, we employ fs-laser-induced filamentation for the *in-situ* generation of the compressed supercontinuum. Two-beam ultrabroadband fs/ps coherent Raman spectroscopy on the ro-vibrational spectra of O_2 and CO_2 is demonstrated in the hot flue gases of a standard laminar premixed CH_4/air flame, at temperatures higher than 2000 K, allowing for simultaneous thermometry and relative O_2/CO_2 concentration measurements.

2. Experimental setup

2.1. Two-beam femtosecond/picosecond CARS setup

The experimental setup for two-beam fs/ps coherent Raman thermometry is detailed in [16] and depicted in Fig. 1; in the following a brief summary of the main features of the system is given. The two laser pulses employed are provided by a single regenerative amplifier system (Astrella, Coherent), operating at 1 kHz and providing an overall pulse energy of 7.5 mJ at 800 nm. The temporally uncompressed output of the amplifier is split 65%–35%: the larger portion is compressed before being fed to a second-harmonic bandwidth compressor (SHBC, Light Conversion), providing a 5 ps duration pulse at 402.7 nm, to serve as the probe pulse. A spatial 4f-filter in transmission, placed in the probe beam path, allows for tuning the duration of the pulse: in

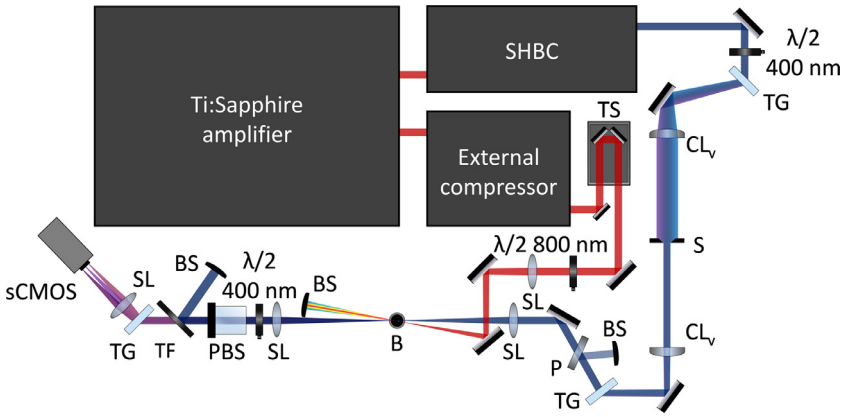

Fig. 1. Schematic of the ultrabroadband two-beam CSRS system. The output of a 1 kHz Ti:Sapphire regenerative amplifier system is split 65%–35% to feed a second-harmonic bandwidth compressor (SHBC) and an external compressor, respectively. The transform-limited 35 fs duration output of the external compressor is focused by a 500 mm focal-length spherical lens (SL) resulting in fs-laser-induced filamentation. The ultrabroadband pump/Stokes beam is crossed by the probe beam at a distance of ~4 mm after exiting the filament: the resulting probe volume is located over the Bunsen burner (B). The ultrabroadband CSRS signal is collected in a coherent imaging spectrometer and imaged to a sCMOS detector. TG, transmission gratings; S, slit; CL_v, cylindrical lenses with vertical alignment symmetry axis; TS, automated translation stage; λ/2, half-wave plates; P, polarizer; PBS, polarization beam splitter; TF, angle-tuneable band-pass filter; BS, beam stop.

the present work, a ~6.6 ps duration probe pulse is employed, with ~300 μJ/pulse. The second output beam is compressed by an external compressor unit providing a transform-limited 35 fs duration pump/Stokes pulse, with 2.3 mJ/pulse. The external compressor furthermore provides an active control on the pulse dispersion, allowing for pulse pre-chirping, to compensate for the effect of group velocity dispersion of the different optical media along the beam path. The use of a single regenerative amplifier to provide all the laser pulses has the advantage of the pulses being automatically synchronised with no temporal jitter. The path-length difference between the pump/Stokes and the probe pulses is compensated for by an optical delay line, and the probe delay is set by the position of an automated translation stage (Thorlabs), with a resolution <10 fs. Half-wave plates for 800 nm and 400 nm (Eksma Optics) are employed to control the orientation of the linearly-polarized pump/Stokes and probe pulses, respectively. In order to ensure the same polarization of the different spectral branches in the CSRS signal, the probe polarization is set parallel to the pump/Stokes: under this condition, both the CO_2 and O_2 Q-branch and the ro-vibrational O_2 O- and S-branch have the same polarization as the pump/Stokes and probe pulses [36,37]. The pump/Stokes and probe beams are both focused at the measurement location by spherical lenses and crossed according to the phase-matching scheme demonstrated in [38]. The probe pulse is focused by a 300 mm focal-length lens, resulting in a measured beam waist of ~30 μm ($1/e^2$), and its energy at the measurement location is measured to be 194 μJ; the pump/Stokes pulse energy, focused by a 500 mm focal-length lens, is measured to be 1.6 mJ. The extremely high peak irradiance (estimated to be ~4.46×10^{14} W/cm^2) of the fs pulse results in the non-linear self-focusing of the pulse (Kerr effect) and the multiphoton ionization of the gas medium, producing a visible plasma channel (i.e. the filament), which can be observed near the focal plane of the focusing lens. This process is also accompanied by the non-linear self-phase modulation of the pulse, resulting in supercontinuum generation and providing, at the measurement location, an ultrabroadband pump/Stokes pulse. The interaction length is estimated by measuring the beam crossing angle (~5°) and the divergence of the beam out of the filament, yielding a pump/Stokes beam waist of ~130 μm ($1/e^2$) at the probe volume location. The probe volume is thus measured to be ~60 μm (width, $1/e^2$) × 3.3 mm (length, $1/e^2$) × ~60 μm (height, $1/e^2$), and is located ~4 mm after the filament. The details of the fs-laser-induced filamentation and of the resulting compressed ultrabroadband pulse are discussed in Section 2.2.

The co-propagating probe beam and CSRS signals are collected by a collimating lens (f:=400 mm). The angle-tuning of a spectral band-pass filter (Semrock) is used to suppress the probe beam and select the spectral window of interest (~1200–1600 cm^{-1}) and a 400 nm half-wave plate (Eksma Optics) turns the polarization of the CARS signal to maximize the diffraction efficiency of a high-resolution transmission grating (3040 lines/mm, Ibsen Photonics). The dispersed signal is then collected by an imaging lens (f:=200 mm) onto a cropped region (100 × 2048 pixels) of the sCMOS detector (Zyla 4.2, Andor) frame, providing 1 kHz frame-rate signal acquisition.

2.2. Compressed supercontinuum generation

In order to achieve the ultrabroadband excitation of the ro-vibrational Raman coherences, we employ a pulse compression technique based on *in-situ* filamentation, as demonstrated in [22]. The propagation of ultrashort pulses in any dielectric medium is accompanied by several nonlinear effects such as Kerr effect, self-phase modulation, and multiphoton ionization [39]. The Kerr effect causes a transient increase of the refractive index of the optical medium at high-pulse intensity, resulting in the self-focusing of the laser beam and the self-phase modulation of the pulse, leading to the generation of new spectral components. Above an input pulse energy threshold of ~40 μJ (corresponding to an estimated irradiance of ~1.14×10^{13} W/cm^2), a fraction of the molecules is ionized through multiphoton absorption (11 photons for N_2 [40] and 8 photons for O_2 [41], at 800 nm laser wavelength) reducing the refractive index and causing self-defocusing of the laser beam. The competition between self-focusing and self-defocusing occurs until the pulse energy, consumed in multiphoton ionization, is sufficient to maintain the nonlinear optical processes. Moreover, the complex dispersion of the ionized gas medium causes self-pulse compression, which may result in pulse durations as low as <5 fs with sufficiently long filaments [42]. In this work we employ relatively fast focusing of the pump/Stokes femtosecond pulse with f:=500 mm, with the Gaussian beam diameter being ~10.5 mm ($1/e^2$) and the pulse energy being ~1.6 mJ, producing a visible filament with a measured length of ~13.2 mm ($1/e^2$). The longitudinal spatial jitter of the filament is assessed by detecting the initiation and the ending point of the visible filament in a sample of 300 single-shot images, and it is measured to be ~350 μm and ~300 μm, respectively. We characterise the supercontinuum generation by measuring the pulse energy of the ultrabroadband pulse, output by the filament, as a function of the input energy of the 35

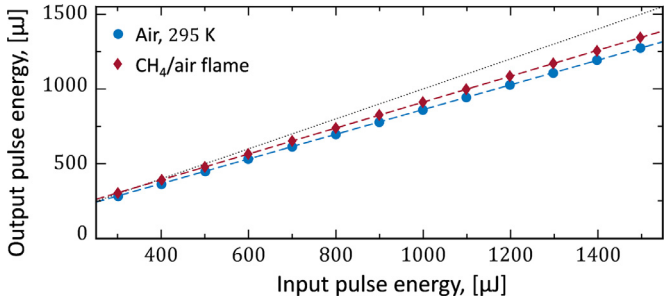

Fig. 2. Power scaling of the ultrabroadband pump/Stokes pulse output by the filament generated in room-temperature air and in the products of a laminar premixed methane/air flame. The pulse energy is measured after the filament collapse: for varying input pulse energy in the range 0.3–1.5 mJ, before the filament initiation, the energy of the compressed ultrabroadband pulse out of the filament scales linearly. The dotted line represents the ideal limit when no pulse energy is lost to the filamentation process.

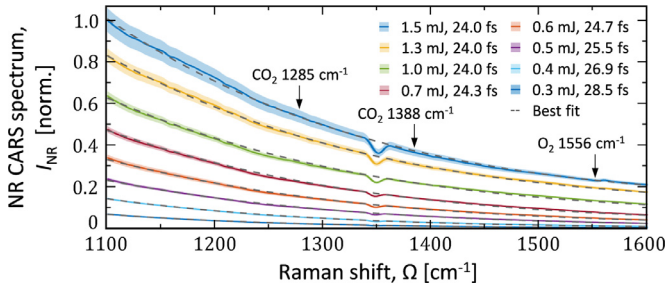

Fig. 3. Averaged NR CSRS spectrum acquired in room temperature argon generated with 0.3–1.5 mJ pump/Stokes pulse energy and the theoretical curve corresponding to 24–28.5 fs pulse duration. The coloured area represents the standard deviation of the NR spectrum over 300 single-shot acquisitions. The visible dip in the NR CSRS spectrum at ~1350 cm^{-1} is due to interference with the N_2^+ fluorescence emission from the filament (see e.g., [45]).

fs duration pulse, measured before the initiation of the filament. Figure 2 illustrates the dependence of the ultrabroadband pulse energy on the energy of the fs laser pulse, for the filament generated in room-temperature air and in the product gases of a laminar premixed CH_4/air flame. The energy output of the filament scales linearly with the energy of the input laser pulse over the whole measured range of 0.3–1.5 mJ, with the energy-conversion efficiency of the supercontinuum generation being ~82% in air and ~86% in the flame (see Fig. 2). The higher energy conversion of the filamentation process in the flame is explained by the ionization rate of the gas medium being larger in the denser room-temperature air than in the hot flame products. The increment of the input energy, from 0.3 mJ to 1.5 mJ, leads to higher irradiance and an earlier onset of the Kerr effect, resulting in the elongation of the filament towards the laser focusing lens, while the location of the ending point of the filament is unaltered: therefore, the probe volume is always maintained at a fixed distance from the filament. Although the filament is partly generated inside the flame, the coherent Raman signal is generated on a ps timescale, so that the molecular ensemble probed in the measurement is not affected by the perturbation of the flame introduced by the ionization process. Furthermore, the electron-ion recombination timescale is in the order of nanoseconds [39], which is much faster than the repetition rate of the regenerative amplifier system, operating at 1 kHz. Hence, even if multiple laser-shots are averaged in the signal acquisition, each measurement is unaffected by the filament generated by the previous laser-shot. In this respect, coherent Raman spectroscopy with ultrabroadband femtosecond laser excitation generated *in-situ* can be claimed to be a non-intrusive diagnostic technique for gas-phase measurements.

In the present work, we demonstrate the *in-situ* generation and *in-situ* use of the filament to compress the pump/Stokes pulse and excite the ro-vibrational Raman transitions of O_2 and CO_2 in the range 1200–1600 cm^{-1}, on the Stokes side. The choice of acquiring the CSRS signal rather than the CARS is motivated by the intensity of the former being significantly larger: at room temperature, the O_2 Q-branch spectrum was detected with two orders of magnitude higher intensity on the Stokes side than on the anti-Stokes side. This is in contrast with the predicted theoretical ratio of the CARS and CSRS signals, which is computed to be ~1.29, owing to the higher carrier frequency of the CARS signal [43]. The observed enhancement in the CSRS signal intensity can be partly attributed to the quantum efficiency (QE) of the sCMOS detector. According to the QE curve reported by the manufacturer, at 1556 cm^{-1}, i.e. at the fundamental band of the O_2 Q-branch spectrum, the QE is approximately 1.75 times higher on the Stokes side than on the anti-Stokes side. In addition, the diffraction efficiency of the transmission grating employed in the coherent imaging spectrometer (see Section 2.1) is reduced on the anti-Stokes side by a factor of ~1.20, according to the diffraction efficiency curve reported by the manufacturer. Finally, we report an asymmetric excitation profile delivered by the ultrabroadband pump/Stokes pulse, as mapped by the non-resonant (NR) signal recorded on the Stokes and anti-Stokes sides: the NR CSRS spectrum at 1556 cm^{-1} is ~20 times higher than the NR CARS spectrum measured at the same Raman shift (see Supplementary Figure S1). Additional experiments are required to explain the asymmetric excitation profile observed in coherent Raman spectroscopy with ultrabroadband femtosecond laser excitation generated *in-situ*.

We estimate the duration of the self-compressed pump/Stokes pulse using the NR CSRS signal. This signal is routinely employed in CARS spectroscopy to map the frequency-dependant excitation efficiency of the Raman coherence: the standard experimental protocols thus entail the generation of the NR CSRS signal from the electronic susceptibility in argon, by setting zero-delay time between the pump/Stokes and probe pulses. The third-order polarization induced by the electronic susceptibility of the optical medium can be estimated as [44]:

$$P_{NR}^{(3)}(t) \propto \left(-\frac{i}{\hbar}\right)^3 E_{12}^*(t)E_{12}(t)E_3(t) \quad (1)$$

where E_{12} and E_{12}^* are the envelopes of the pump/Stokes pulse and its complex conjugate, E_3 is the probe pulse envelope. The spectrum of the NR CSRS signal can then be computed as the Fourier transform of $P_{NR}^{(3)}(t)$. The compressed time-domain pump/Stokes pulse envelope (E_{12}) is assumed to be transform-limited (TL) and to have a Gaussian profile, with the pulse duration being a fitting parameter to determine the pulse compression in the filament. The time-domain envelope of the probe pulse (E_3) is measured experimentally, by performing a probe delay-scan in room-temperature argon, employing a pump/Stokes pulse energy below the filamentation threshold. Figure 3 shows the NR CSRS spectra (averaged over 300 single-shots) acquired for a pump/Stokes pulse energy varying between 0.3 and 1.5 mJ and the fit to the theoretical spectra computed according to Eq. (1). The increase of the pulse energy leads to a stronger self-phase modulation, resulting in a larger bandwidth of the laser pulse at the output of the filament, as shown by the increased excitation efficiency at larger Raman shifts. The fit to the theoretical NR spectrum simulated for a Gaussian TL pulse shows the corresponding temporal compression of the pump/Stokes pulse from 28.5 fs to 24 fs. A plateau in the pulse compression is reached at ~1 mJ/pulse: increasing the pulse energy above this threshold does not result in a further compression of the pulse, but only increases the electronic Raman coherence, enhancing the NR signal intensity. The experimental NR spectra presented in Fig. 3 show a consistent dip at ~1350 cm^{-1} due to the destructive interference at the detector of the NR CSRS signal

and the fluorescence signal produced by the N_2^+ ions generated in the filament [45,46]. The shot-to-shot fluctuations in the overall energy of the pump/Stokes pulse output by the filament stay within ~0.5% and the relative standard deviation of its bandwidth, evaluated in the region 1200–1600 cm^{-1}, is below 10%.

2.3. Bunsen burner

We performed ultrabroadband two-beam fs/ps coherent Raman spectroscopy in a quasi-adiabatic laminar premixed CH_4/air flame, provided on a Bunsen burner. The burner consists of a seamless stainless steel pipe with ~12 mm inner diameter and a length-to-diameter ratio (~100:1) chosen to dampen coherent flow structures at the exit plane. The fuel and the oxidizer are provided by separated pressurised vessels and the flows are independently controlled by rotameters (Omega), and mixed afterwards to deliver the combustible mixture to the burner. The volumetric flow rate is maintained below 5 standard litre per minute (SLPM): the Reynolds number is thus computed to be <1000, resulting in a laminar flow. The probe volume is placed ~ 7 mm above the tip of the conical flame. The equivalence ratio of the combustible mixture is varied in the fuel-lean regime from φ=0.6 to slightly fuel rich conditions (φ=1.05), to simultaneously acquire the CSRS spectra by O_2 and CO_2. In correspondence of the two leanest cases tested, the flame is stabilized as a V-shaped flame to avoid lean blow-off, employing a 4 mm diameter steel rod placed at a height of ~12 mm above the burner rim; in these flame conditions the probe volume is placed ~5 mm above the rod.

3. Time-resolved CSRS model

3.1. Ro-vibrational fs/ps CSRS processes

The principles underlying the time-domain modelling of the fs/ps coherent Raman scattering process have been thoroughly elaborated upon in the literature (e.g., [47–50]), for both pure-rotational and ro-vibrational CARS: in the following, we provide only a brief summary of the main assumptions and equations employed. In the present work, we report on the experimental acquisition of CSRS spectra; however, from a theoretical perspective, the time-resolved model of the ro-vibrational O_2-CO_2 CARS spectra can be readily extended to simulate the CSRS spectra, under electronically non-resonant conditions [51,52].

The third-order polarisation resulting from the FWM process can be described, in the time domain, as the convolution of the envelopes of the input electromagnetic fields with the ordinary response function of the gas-phase medium, represented by its macroscopic electric susceptibility $\chi^{(3)}$ [14,49]:

$$P^{(3)}(t,\ t_{12},\tau_{23},t_3) = \left(-\frac{i}{\hbar}\right)^3 \int_{-\infty}^{t} dt_3 \int_{-\infty}^{t_3} dt_{12}\, \chi^{(3)} \times (t,t_3,t_{12}) E_3(t-t_3) e^{i(\omega_1-\omega_2+\omega_3)t_3} \times E_{12}^*(t+\tau_{23}-t_3-t_{12}) e^{i(\omega_1-\omega_2)t_{12}} E_{12}(t+\tau_{23}-t_3-t_{12}) e^{i\omega_1 t_{12}} \quad (2)$$

where ω_i is the frequency of the i th photon (with index i = 1, 2 and 3 corresponding to the pump, Stokes and probe photons, respectively), E_{12} and E_{12}^* are the envelopes of the pump/Stokes pulse and its complex conjugate, E_3 is the envelope of the probe pulse, t_{12} is the coherence timescale between the pump/Stokes and probe pulse, t_3 is the coherence timescale in the scattering of the probe pulse, and τ_{23} is the delay of the probe pulse relative to the pump/Stokes pulse. Under the assumptions of instantaneous dephasing of the electronic coherence in non-resonant single-photon interactions, and of infinite bandwidth of the pump/Stokes excitation pulse [44], Eq. (2) is greatly simplified as:

$$P^{(3)}(t) = \left(-\frac{i}{\hbar}\right)^3 E_3(t-t_3)\chi^{(3)}(t) \quad (3)$$

Under these assumptions, the conceptual core in the fs/ps CSRS model is represented by the third-order non-linear susceptibility of the optical medium. This term is typically treated phenomenologically [47], as the weighted sum of dampened oscillations at the frequencies corresponding to the transitions in the ro-vibrational energy manifold of the Raman-active species in the medium:

$$\chi^{(3)}_{\mathrm{CSRS}}(t) = \sum_k \sum_v \sum_J \mathrm{X}_k I^{(k)}_{(v_\mathrm{f}J_\mathrm{f})\leftarrow(v_\mathrm{i}J_\mathrm{i})} \exp\left[\left(i\omega^{(k)}_{(v_\mathrm{f}J_\mathrm{f})\leftarrow(v_\mathrm{i}J_\mathrm{i})} - \Gamma^{(k)}_{(v_\mathrm{f}J_\mathrm{f})\leftarrow(v_\mathrm{i}J_\mathrm{i})}\right)t\right] \quad (4)$$

where X_k is the mole fraction of the k-th species considered, $I_{(v_\mathrm{f}J_\mathrm{f})\leftarrow(v_\mathrm{i}J_\mathrm{i})}$ is the strength of the spectral line corresponding to the Raman transition between the initial $(v_\mathrm{i}, J_\mathrm{i})$ and the final energy state $(v_\mathrm{f}, J_\mathrm{f})$, which carries the temperature sensitivity of the Raman spectrum as a dependence on the Boltzmann distribution over these ro-vibrational energy states. $\omega^{(k)}_{(v_\mathrm{f}J_\mathrm{f})\leftarrow(v_\mathrm{i}J_\mathrm{i})}$ and $\Gamma^{(k)}_{(v_\mathrm{f}J_\mathrm{f})\leftarrow(v_\mathrm{i}J_\mathrm{i})}$ are, respectively, the frequency and the dephasing coefficient of the Raman transition, representing the position and the linewidth (full-width-at-half-maximum, FWHM) of the corresponding spectral line in the frequency domain. The strength of the ro-vibrational Raman lines is computed according to [4,15]:

$$I_{(v,J)\leftarrow(v+1,J)} = \left[F_\alpha^{(k)}\left(\alpha^{(k)}_{(v,J)\leftarrow(v+1,J)}\right)^2 + \frac{4}{45}F_\gamma^{(k)} b^{(k)}_{J,J}\left(\gamma^{(k)}_{(v,J)\leftarrow(v+1,J)}\right)^2\right] N^{(k)}\Delta\rho_{(v,J)\leftarrow(v+1,J)}$$
$$I_{(v,J)\leftarrow(v+1,J\pm2)} = \frac{4}{45}F_\gamma^{(k)} b^{(k)}_{J,J\pm2}\left(\gamma^{(k)}_{(v,J)\leftarrow(v+1,J\pm2)}\right)^2 N^{(k)}\Delta\rho_{(v,J)\leftarrow(v+1,J\pm2)} \quad (5)$$

where $\alpha^{(k)}_{(v_\mathrm{f}J_\mathrm{f})\leftarrow(v_\mathrm{i}J_\mathrm{i})}$ and $\gamma^{(k)}_{(v_\mathrm{f}J_\mathrm{f})\leftarrow(v_\mathrm{i}J_\mathrm{i})}$ are the isotropic and anisotropic invariants of the (transition) polarizability tensor, $b^{(k)}_{J_\mathrm{f},J_\mathrm{i}}$ is the Placzek-Teller coefficient for the rotational transition ($J_\mathrm{f} \leftarrow J_\mathrm{i}$), $F^{(k)}_{\alpha/\gamma}$ are the Herman-Wallis factors for isotropic/anisotropic transitions, $N^{(k)}$ is the number density of the k-th species, and $\Delta\rho_{(v_\mathrm{i},\ J_\mathrm{i})\rightarrow(v_\mathrm{f}J_\mathrm{f})}$ is the differential Boltzmann distribution between the initial and the final energy states. The summations in Eq. (4) are intended over all the Raman-active species (k), and for all the ro-vibrational energy levels (v, J) that are significantly populated in the thermal ensemble. The labels "v" and "J" are employed here to represent the quantised vibrational and rotational levels in the energy manifold of a certain species. In reality, more than two quantum numbers might be required to completely characterise the quantum state of a specific molecule: this is the case e.g. for CO_2.

The phenomenological model represented by Eq. (4) can thus be employed to compute the non-linear optical response of the gas-phase medium, for different input values of its temperature and composition. By combining this response with the experimentally-measured envelope of the probe pulse, one can

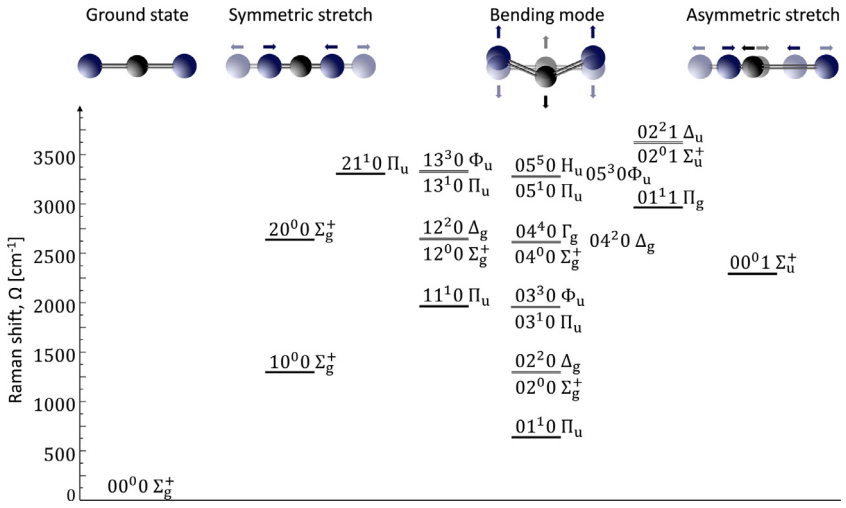

Fig. 4. Energy diagram detailing the structure of the vibrational energy manifold for the CO_2 molecule up to 3500 cm^{-1}. The vibrational energy state of the molecule is described by four quantum numbers, $v_1v_2lv_3$, according to the notation in [53]: v_1 is the symmetric stretch quantum number, v_2 is the bending mode quantum number, l is the vibrational angular momentum quantum number, and v_3 is the asymmetric stretch quantum number.

simulate the ro-vibrational CO_2 and O_2 Raman spectra for temperatures and compositions relevant to combustion studies.

3.2. Ro-vibrational CO_2 spectrum

In order to synthesise the ro-vibrational Q-branch spectrum of CO_2, an accurate description of the structure of its ro-vibrational energy manifold is required. CO_2 is a triatomic molecule made of two oxygen atoms and a carbon atom forming two double covalent bonds: the resulting molecule is linear and centrosymmetric. This structure results in three distinct normal vibrational modes: the symmetric stretch, the scissoring bend and the asymmetric stretch mode (see inlet in Fig. 4). Because of the point-symmetry of the molecule, the symmetric stretch is the only Raman-active mode, while the bending and asymmetric mode are IR-active only. The vibrational energy states of the CO_2 molecule can thus be labelled, according to the notation in Herzberg [53], as $v_1v_2lv_3$, where v_1 is the symmetric stretch quantum number, v_2 is the bending quantum number, l is the vibrational angular momentum quantum number, and v_3 is the asymmetric stretch quantum number. The vibrational angular momentum is due to the asymmetric motion of the nuclei with respect to the inter-nuclear axis in the bending mode, resulting in a rotational motion about the (equilibrium) inter-nuclear axis [15,53,54]. This additional angular momentum is quantized, with quantum number l=-v_2,-v_2+2,...,v_2−2,v_2. The energy levels associated to the bending mode are therefore (v_2+1)-fold degenerate and the corresponding ro-vibrational energy is computed according to [54]:

$$E(v,J) = G_v + B_v\left[J(J+1) - l^2\right] - D_v\left[J(J+1) - l^2\right]^2 + H_v\left[J(J+1) - l^2\right]^3 \quad (6)$$

where G_v, B_v, D_v and H_v are the spectroscopic constants of CO_2 (with $v = v_1v_2lv_3$), and J is the total angular momentum quantum number, which includes the contribution of the vibrational angular momentum, so that $J \geq |l|$ [15,54]. In addition, as the vibrational angular momentum is parallel to the inter-nuclear axis, when it is in a degenerate bending state, CO_2 behaves as a prolate symmetric top molecule [15], and the Placzek-Teller coefficients for the corresponding Raman band are computed as:

$$b(J,l) = \frac{\left[J(J+1) - 3l^2\right]^2}{J(J+1)(2J-1)(2J+3)} \quad (7)$$

The ro-vibrational Q-branch CARS spectrum of CO_2 is thus made of the spectral lines corresponding to the excitation of the symmetric stretch mode, according to the selection rules: Δv_1=1, Δv_2=Δv_3=Δl=0. Vibrational states characterised by an active bending mode (i.e. for v_2≠0) are (v_2+1)-fold degenerate, as the vibrational angular momentum has quantized values l=-v_2,-v_2+2,...,v_2−2,v_2. Each degenerate bending mode accompanied by vibrational angular momentum (i.e. for l≠0) is double-degenerate and, in analogy with the Λ-type doubling due to spin-orbit interaction, capital Greek letters are used to label these states, as shown in Fig. 4. Moreover, when two different vibrational states characterised by the same vibrational wave function symmetry have similar energy, their respective wave function can “mix”, a phenomenon known as Fermi resonance [32,55]. As the unperturbed (i.e. as described by a harmonic potential Hamiltonian) v_1 and $2v_2$ states have almost identical energy, due to Fermi resonance the IR-active $2v_2$ lines appear in the Raman spectrum and the anharmonic terms in the exact Hamiltonian result in the “repulsion” of the spectral lines in the v_1+$2v_2$ dyad [54].

The ro-vibrational CO_2 fs/ps CARS model developed in the present work employs the ro-vibrational constants given in [56], to compute the molecular energy according to Eq. (6). In the thermal ensemble, these energy levels are populated as described by Boltzmann distribution:

$$\rho(v,J) = g_S\, g_v\, g_J \frac{\exp(-E(v,J)/(k_B T))}{Z} \quad (8)$$

where k_B is the Boltzmann constant, T is the temperature, Z is the partition function, $g_J = 2J+1$ is the rotational degeneracy, g_v is the vibrational degeneracy, and g_S is the nuclear spin degeneracy. The latter is respectively 1 and 0 for even and odd rotational states in those vibrational bands characterised by an even symmetry of the nuclear wave function (e.g. in the vibrational ground state), while the opposite holds for odd-symmetric states. As the temperature increases, higher energy states became substantially populated in the vibrational Boltzmann population of CO_2. The values of the transition polarizability isotropic (α) and anisotropic (γ) invariants are required to compute the Raman line-strengths in Eq. (5). Lemus et al. [57] used an algebraic approach to compute the vibrational transition dipole moments of CO_2: their calculations are in good agreement with experimental values in [58]. The resulting polarizability transition moments for ro-vibrational transition in the range 1100–1600 cm^{-1} are employed extensively in the present work. On the other hand, no reliable measurement of the dependence of the

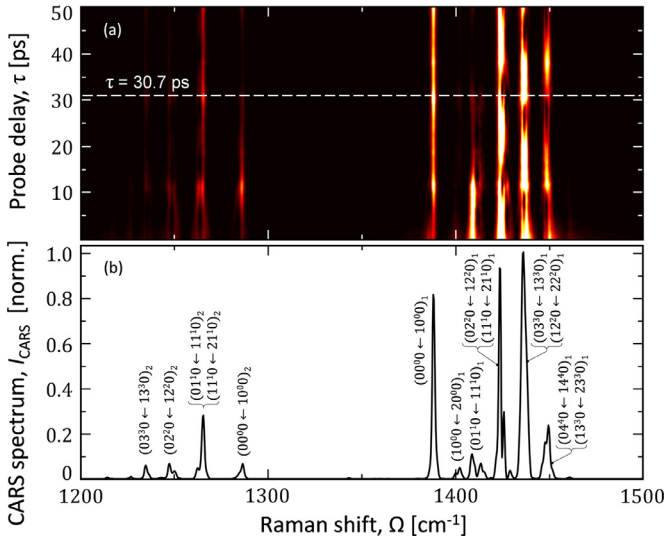

Fig. 5. (a) Spectrochronogram of the ro-vibrational CO_2 Q-branch spectrum, simulated by the time-domain CSRS code for an input temperature of 2200 K and an experimental probe duration measured to be 6.6 ps. The simulated fs/ps CO_2 CSRS spectrum is affected by a severe beating of all the spectral lines, due to the unresolved transitions between the many ro-vibrational energy states populated at flame temperature. (b) CO_2 Q-branch spectrum simulated for a probe delay of 30.7 ps. The main ro-vibrational bands contributing to the unresolved spectral lines are reported, the labelling follows the notation in [34].

transition dipole moments on the rotational energy state could be found in the literature, and the same values of $\alpha_{v+1\rightarrow v}$ are employed for all the rotational lines within the same vibrational band [59]. To the best of our knowledge, the anisotropic polarizability $\gamma_{v+1\rightarrow v}$, is also not known with sufficient accuracy: in absence of accurate experimental data or computations, the CO_2 model only includes the isotropic contribution to the Q-branch CO_2 spectrum. This assumption is justified by the well-established value of the depolarization ratio of the fundamental vibrational band in the CO_2 Raman spectrum at 1388 cm^{-1}, amounting to 0.027 [60]. The spectral model includes temperature-dependant linewidths for self-broadened CO_2 and for CO_2 perturbed by N_2, as this is the most abundant species in air-fed combustion. The linewidths are fitted, according to the modified exponential energy-gap (MEG) scaling law [61], from the experimental data reported in [24] for the self-broadened CO_2 spectral lines; the collisional broadening due to nitrogen, on the other hand, is modelled according to [62].

Figure 5 shows the ro-vibrational Q-branch spectrum of CO_2, in the spectral range 1200–1500 cm^{-1}, simulated by the time-domain CARS code, for an input temperature of 2200 K and assuming a probe duration of 6.6 ps. The spectrochronogram in Fig. 5(a) reveals the strong beating of the vibrational hot bands due to unresolved ro-vibrational lines pertaining to different vibrational transitions: these unresolved vibrational bands are identified in Fig. 5(b), and labelled according to the notation in Herzberg. The structure of the Fermi resonances between the v_1 and $2v_2$ vibrational bands is clearly visible and identified in the labels by the subscripts. The fundamental band corresponding to the first symmetric stretch is the Fermi dyad, comprising a lower-frequency spectral line located at 1285 cm^{-1} (referred to the "red" branch of the dyad [63]), and a higher-frequency line at 1388 cm^{-1} (the "blue" branch of the dyad [64]). The beating of the spectrum with the probe pulse delay is particularly evident on the second, third and fourth hot bands on the blue Q-branch spectrum (spanning the spectral region >1350 cm^{-1}), which are characterised by similar beating patterns, with a period of about 36 ps. This behaviour is explained by the close separation (~0.2 cm^{-1}) of two distinct vibrational bands, in each spectral peak, being smaller than the probe bandwidth (~2.23 cm^{-1}). In this respect, the use of a single regenerative amplifier system, providing automatically synchronised pump/Stokes and probe beam pulses at the measurement location, can improve the single-shot precision of vibrational CO_2 coherent Raman thermometry.

3.3. Ro-vibrational O_2 spectrum

Compared to CO_2, the oxygen molecule presents a much simpler energy manifold: molecular vibration is only possible along the direction of the inter-nuclear axis: only one quantum number (v) is thus required to describe the vibrational energy state of O_2. On the other hand, the ground electronic state of O_2 ($X\ ^3\Sigma_g^-$) is characterised by unpaired electrons [65,66], resulting in an electronic spin angular momentum quantum number $S = 1$: the coupling of this angular momentum component to the nuclear angular momentum (with quantum number N) is accounted for by adopting the Hund's case (b) [53]. Under such conditions, the total angular momentum J is the direct sum of the electronic spin and nuclear components, $J = N + S$, resulting in each energy state with nuclear angular momentum N, being a triplet with $J = N$, $N \pm 1$. Courtney and Kliewer [67] experimentally demonstrated the effect of this coupling on the S-branch Raman spectrum: a significant temporal beating was measured the time-resolved hybrid fs/ps CARS signal, for probe delays larger than 100 ps. In the present work, the ro-vibrational time-domain model of the O_2 CSRS spectra is simplified by considering the triplets as degenerate states: this assumption is justified by the lower transition frequency separation for the ro-vibrational Q-branch lines, with respect to the O- and S-branch lines [23], and the relatively short probe delay of ~31 ps employed in the flame experiment. The energy of a molecule in the ro-vibrational state (v, J) is thus described by a simplified form of Eq. (6), as:

$$E(v,J) = G_v + B_v[J(J+1)] - D_v[J(J+1)]^2 + H_v[J(J+1)]^3 \qquad (9)$$

The ro-vibrational constants of diatomic oxygen in the ground electronic state can be found in [23]. Eq. (8) and (9) are used to compute the differential Boltzmann population for the ro-vibrational Q-, O- and S-branch Raman transitions. Placzek-Teller coefficients are computed for the line strengths of the Q-, O- and S-branch spectra respectively, as [15]:

$$\begin{aligned} b_{J\leftarrow J-2}(J) &= \frac{3J(J-1)}{2(2J+1)(2J-1)} \\ b_{J\leftarrow J}(J) &= \frac{J(J+1)}{(2J-1)(2J+3)} \\ b_{J\leftarrow J+2}(J) &= \frac{3(J+1)(J+2)}{2(2J+1)(2J+3)} \end{aligned} \qquad (10)$$

According to Eq. (5), the intensity of the spectral lines furthermore depends on the Herman-Wallis factor, and on the isotropic (α) and anisotropic (γ) invariants of the transition polarizability tensor, here computed according to the formulae provided in [68]. The spectral linewidths employed in the model account for the collisional broadening due to self-perturbed O_2 and for the O_2-N_2 collisional system. The temperature-dependant Q-branch linewidths are determined by applying the MEG law to the experimental data reported by Millot et al. [69] for both O_2-O_2 and O_2-N_2 collisional broadening. The linewidths of the ro-vibrational O_2 O- and S-branch spectra are computed from the Q-branch linewidths, by applying the random phase approximation [70].

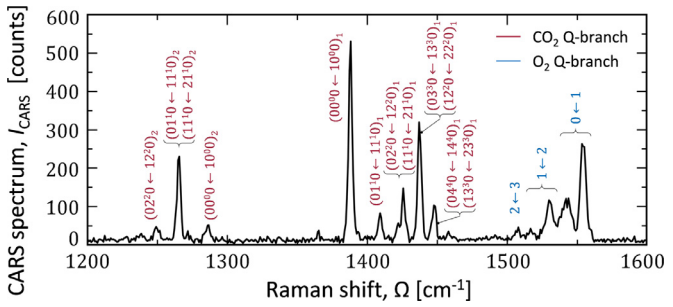

Fig. 6. Single-shot O_2-CO_2 CSRS spectrum acquired in the products of a laminar premixed CH_4/air flame (φ=0.77). The red labels denote the Q-branch CO_2 transitions according to the notation in [53]; blue labels are employed to indicate the fundamental and hot band transitions in the O_2 Q-branch spectrum.

4. Results and discussion

4.1. O_2-CO_2 coherent Raman spectroscopy in a laminar premixed CH_4/air flame

We demonstrate the use of ultrabroadband coherent Raman spectroscopy, over the spectral range 1200–1600 cm^{-1}, to perform thermometry and relative O_2/CO_2 concentration measurements in a typical hydrocarbon flame. As discussed in Section 2.3, the measurements were performed in the products of a laminar premixed CH_4/air flame, provided on a Bunsen burner: six different values of the equivalence ratio, from 0.6 to 1.05, were tested in the flame experiments.

An example of a single-shot ro-vibrational O_2-CO_2 CSRS spectrum, acquired in the products of the laminar premixed CH_4/air flame (φ=0.77), is depicted in Fig. 6. The three peaks visible in the range ∼1200–1300 cm^{-1} represent the "red" CO_2 Q-branch spectrum, consisting of the fundamental and the first three hot bands; the "blue" CO_2 Q-branch lies in the spectral region from the fundamental transition at 1388 cm^{-1} to ∼1450 cm^{-1}, with many vibrational bands convolved with each other and giving rise to the beating patterns simulated in Fig. 5(a). The ro-vibrational O_2 Q-branch is positioned at larger Raman shifts and consists, at the present temperature, of the fundamental band –labelled as "0←1", according to the change in its only vibrational number–, and the first two hot bands. The signal-to-noise ratio (SNR) of the single-shot spectra acquired at this flame condition is measured to be ∼48, employing full-vertical binning and a factor of 2 horizontal binning (effective pixel width of 11 µm) as the acquisition mode. A sample of one thousand single-shot spectra, acquired in these flame conditions, is fitted to the theoretical models discussed in the previous section to extract the temperature and the relative O_2/CO_2 concentration. The temperature assessed from the CO_2 spectrum is 1921 K with a standard deviation of 27 K, which, compared to the adiabatic flame temperature (1951 K), result in an accuracy of −1.5% and a single-shot precision of 1.4%. The O_2 thermometry yields an average temperature of 1749 K, with a standard deviation of 81 K, corresponding to an accuracy of −11.6% and a single-shot precision of 4.7%. The relative O_2/CO_2 concentration is measured to be 0.66, with a standard deviation of 0.03: the corresponding accuracy and precision are thus assessed to 33.0% and 4.1%, respectively. A significant bias in the measured relative O_2/CO_2 concentration is reported at all flame conditions: this issue is addressed more in the details in Section 4.3.

While single-shot detection of the CSRS signal is possible in all the flame conditions tested in the present work, the SNR is severely affected by the increased temperature, resulting in SNR∼3 at φ=1.05. In order to assess the performance of the time-domain CSRS model at temperatures higher than 2000 K, 40 flame spec-

Table 1
Comparison of the CARS thermometry performed on the ro-vibrational Q-branch spectra of the CO_2 and O_2 molecules in the products of the laminar premixed CH_4/air flame, for the different values of the equivalence ratio. For φ>0.84 the O_2 CSRS signal is too weak to provide a reliable estimation of the gas temperature. The results of ro-vibrational thermometry performed on the 40-shot averaged ro-vibrational CSRS spectra of O_2 and CO_2, are compared to the adiabatic flame temperature and the results of pure-rotational thermometry performed on the single-shot pure-rotational CARS spectra of O_2 and N_2.

Equivalence ratio φ	Adiabatic flame temperature $T_{ad.}$	Pure-rotational N_2-O_2 thermometry			Ro-vibrational CO_2 thermometry			Ro-vibrational O_2 thermometry		
		$T_{avg.}$	$(T_{avg.}-T_{ad.})/T_{avg.}$	$\sigma_T/T_{avg.}$	$T_{avg.}$	$(T_{avg.}-T_{ad.})/T_{avg.}$	$\sigma_T/T_{avg.}$	$T_{avg.}$	$(T_{avg.}-T_{ad.})/T_{avg.}$	$\sigma_T/T_{avg.}$
[-]	[K]	[K]	[%]	[%]	[K]	[%]	[%]	[K]	[%]	[%]
0.60	1669	1622	−2.9	0.4	1619	−3.1	1.5	1636	−2.0	2.0
0.66	1775	1783	+0.5	0.4	1711	−3.7	1.2	1711	−3.7	1.0
0.77	1951	1909	−2.2	0.3	1836	−6.3	1.1	1787	−9.1	1.5
0.84	2059	2019	−2.0	0.4	1939	−6.2	1.1	2045	−0.7	5.4
0.93	2167	2086	−3.9	0.4	2081	−4.1	0.8	–	–	–
1.05	2226	2132	−4.4	0.5	2113	−5.3	0.7	–	–	–

Table 2
Comparison of the CARS relative concentration measurements performed on the ro-vibrational Q-branch spectra of the CO_2 and O_2 molecules in the product of the laminar premixed CH_4/air flame, for the different values of the equivalence ratio. The relative O_2/CO_2 concentrations assessed from the 40-shot averaged ro-vibrational CSRS spectra of O_2 and CO_2 are compared to the values predicted by a one-dimensional laminar flame code [72].

Equivalence ratio φ	Relative O_2/CO_2 concentration $X_{O_2-CO_2}$	Relative O_2/CO_2 CARS measurements		
		$X_{O_2-CO_2}$	ΔX / $X_{O_2-CO_2}$	σ_X / $X_{O_2-CO_2}$
[-]	[-]	[-]	[%]	[%]
0.60	0.97	1.56	+61.2	5.9
0.66	0.75	1.16	+54.4	5.4
0.77	0.44	0.79	+79.9	3.5
0.84	0.28	0.38	+32.9	2.1
0.93	0.13	–	–	–
1.05	0.02	–	–	–

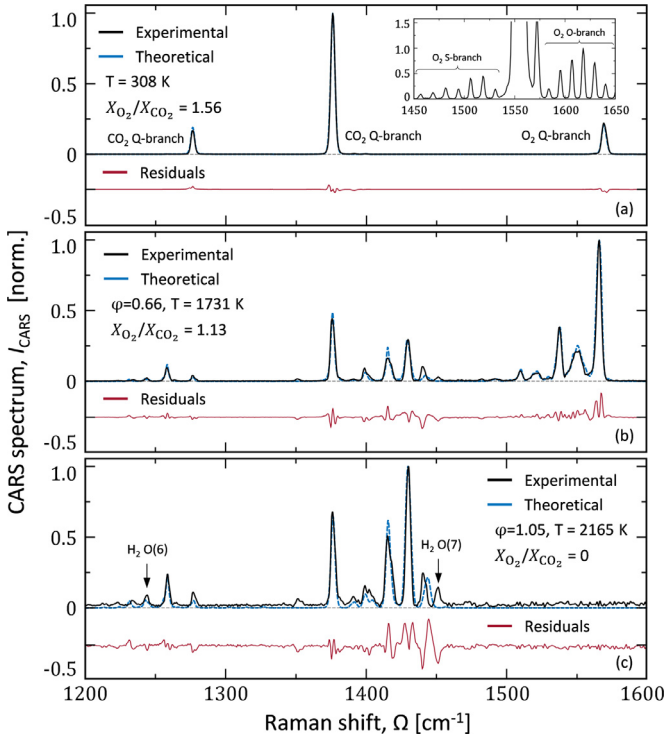

Fig. 7. (a) Single-shot ro-vibrational CO_2 and O_2 CSRS spectra acquired, in the spectral range 1200–1600 cm^{-1}, in a room-temperature CO_2/air mixture (9%–91%). The O_2 CSRS signal is dominated by the Q-branch spectrum, centred at ~1556 cm^{-1}; the CO_2 Q-branch spectrum is represented, at this temperature, by the sole Fermi dyad at 1285 cm^{-1} and 1388 cm^{-1}. The inset shows the ro-vibrational O- and S-branch spectra of O_2, these are two orders of magnitude weaker than the ro-vibrational Q-branch spectrum. (b) 40-shot averaged ro-vibrational CO_2 and O_2 CSRS spectra acquired in the hot product gases of a laminar premixed CH_4/air flame at φ=0.66. (c) 40-shot averaged ro-vibrational CO_2 and O_2 CSRS spectra acquired in the hot product gases of a laminar premixed CH_4/air flame at φ=1.05.

tra are averaged so as to guarantee a sufficient signal level over the whole set of experimental conditions. Therefore, 40-shot averaged spectra are presented in Fig. 7 and employed to assess the ro-vibrational thermometry and relative concentration measurements in Tables 1 and 2, respectively.

Figure 7(a) shows a single-shot ro-vibrational CSRS spectrum acquired in a room-temperature (295 K) air/CO_2 mixture (9%–91%); Fig. 7(b) and (c) show 40-shot averaged CSRS spectra acquired in the product gases of the flame for φ = 0.66 and 1.05, respectively: for better clarity the absolute value of the Raman shift is given on the abscissa. Comparing the Raman spectra in the progression from Fig. 7(a) to Fig. 7(c), one should notice the combined effect of the temperature increment and of the variation in the relative O_2/CO_2 concentrations. At room temperature, only the ground vibrational states of the CO_2 and O_2 molecules are significantly populated so that only one vibrational band can be identified in the resulting Q-branch CSRS spectra. The inset in Fig. 7(a) shows the ro-vibrational O- and S-branch spectra of O_2 detected on the sides of the ro-vibrational Q-branch spectrum. As the corresponding transitions are only due to the anisotropic polarizability of the molecule, as shown in Eq. (5), the ro-vibrational O- and S-branch spectra are two orders of magnitude weaker than the Q-branch spectrum. The O_2 Q-branch spectra in Fig. 7(a) and (b) show a clear temperature dependence as higher vibrational energy states become populated in the Boltzmann distribution, and the corresponding spectral bands appear at lower Raman shifts with respect to the fundamental band centred at ~1556 cm^{-1}. An even stronger temperature dependence is shown by the CO_2 Q-branch spectrum, where the energy states corresponding to all the normal vibrational modes become populated at high temperature: this behaviour is reflected in a number of vibrational spectral bands appearing in both the red and blue Q-branch spectra. At slightly fuel-rich conditions (φ=1.05), O_2 is completely consumed in the chemical reaction and is absent from the CSRS spectra acquired in the flame products; on the other hand, the spectral signature of molecular hydrogen (H_2) appears as a strong spectral line, corresponding to O(7) at ~1447 cm^{-1}, and a much weaker line at 1246 cm^{-1}, corresponding to O(6) [71]. As shown in Fig. 7(c), these lines are overlapped to the CO_2 Q-branch spectrum and skew the experimental spectrum with respect to the synthetic one. This is particularly evident for the O(7) line being approximately stronger than O(6), as the nuclear spin degeneracy of H_2 is respectively 1 and 3 for even and odd values of J; this line was therefore excluded by the spectral fitting routine. The comparison of the experimental and synthetic spectra presented in Fig. 7 moreover shows a mismatch in correspondence of the second and fourth hot bands of the CO_2 blue Q-branch spectrum: this is attributed to the uncertainty in the experimental and computed line positions and transition dipole moments for higher vibrational bands found in the literature, resulting in a different beating pattern between the underlying ro-vibrational transitions.

4.2. Ro-vibrational coherent Raman thermometry

In the present work, CO_2 is employed as the main thermometric species as, being one of the main combustion products, it is present in the hot flue gases in significant concentrations for any equivalence ratio employed in the experiment. The time-domain CO_2 CSRS code was validated by performing coherent Raman thermometry on a sample of one thousand Raman spectra acquired in a room-temperature CO_2/air mixture: the average temperature was estimated to 308 K with a standard deviation of 12 K, resulting in a measurement accuracy of 2.7% and precision of 4.0%.

The relatively low accuracy of the low-temperature ro-vibrational CO_2 thermometry is not surprising as only two lines, corresponding to the Fermi dyad of the fundamental vibrational band, are available for the spectral fitting. In the flame experiment, on the other hand, the CSRS spectra are dominated by a number of spectral lines, corresponding to the ro-vibrational transitions between the many vibrational energy states populated at higher temperatures. Table 1 presents the results of ro-vibrational CO_2 thermometry performed at the six values of the equivalence ratio employed in the experiment: a sample of one thousand CSRS spectra was acquired at each flame condition. The experimental results are validated by the comparison to both the adiabatic flame temperatures and to the temperatures measured by pure-rotational CARS thermometry. The adiabatic flame temperature is predicted for the different values of equivalence ratio by a one-dimensional laminar flame code (CHEM1D [72]), while the single-shot CARS measurements were performed on the pure-rotational spectra of N_2 and O_2 in the spectral region 0–400 cm^{-1} according to [16]. Ro-vibrational CO_2 thermometry shows a reasonable agreement with pure-rotational N_2-O_2 thermometry and with the expected flame temperature: depending on the equivalence ratio considered, the agreement between the pure-rotational N_2-O_2 and ro-vibrational CO_2 thermometry varies between 0.2% (for φ=0.60 and 0.93) and 4% (for φ=0.84). When compared to the adiabatic flame temperature, the accuracy of CO_2 thermometry, quantified in terms of the systematic bias of the experimental temperature, varies between 3.1% (for φ=0.60) and 6.3% (for φ=0.77 and 0.84). These values are in line with those computed for the corresponding RCARS measurements at the same flame conditions, yielding a systematic bias between 0.5% (for φ=0.66) and 4.4% (for φ=1.05). As far as the precision of ro-vibrational CO_2 thermometry is concerned, it is interesting to point out how the relative standard deviation (σ_T/T_{avg}) of the temperature measurements decreases for increasing equivalence ratios and flame temperatures. The corresponding thermometric precision is improved from 1.5% (for φ=0.60) to 0.7% (for φ=1.05). This result is in contrast with the most commonly reported CARS measurements, where in general the precision is negatively impacted by the increasing temperature, which determines a reduction in the number density of the scattering species and, consequently, a degrading SNR [73,74]: indeed, this the case for ro-vibrational CO_2 thermometry as well. At higher equivalence ratio, on the other hand, CO_2 thermometry benefits both from the increased CO_2 concentration and from the much richer ro-vibrational spectrum with pronounced hot bands, resulting in a more robust temperature assessment.

Furthermore, for values of the equivalence ratio below 0.84, the concentration of excess oxygen in the hot products is large enough to experimentally detect the O_2 CSRS signal with a signal-to-noise ratio greater than ~3. As shown in Fig. 7(b), at high temperature the O_2 Q-branch spectrum presents a number of vibrational bands: alongside the fundamental band at ~1556 cm^{-1}, the second and third vibrational hot bands can be identified at ~1532 and ~1509 cm^{-1} [23], respectively. Due to the limited spectral resolution, each vibrational band appears as two distinct peaks in the experimental spectrum (see Supplementary Figure S2). The comparison between the temperature measurements performed on the CO_2 and O_2 CSRS spectra is provided in Table 1, for values of the equivalence ratio up to 0.84. Ro-vibrational thermometry was performed by two independent contour-fitting routines on the ro-vibrational O_2 and CO_2 spectra acquired simultaneously in the 1200–1600 cm^{-1} spectral region. The good agreement of the temperatures measured by independently fitting the spectra of the two chemicals thus provides an additional mean of validation for the time-domain CARS code developed in the present work. As a matter of fact, ro-vibrational CO_2 and O_2 thermometry agree to within 2.7% of the measured temperature for all the considered equivalence ratios, with the only exception of φ=0.84, where the two temperature measurements diverge by 5.5%. At this latter flame condition, the O_2 signal is significantly affected by the reduction in O_2 concentration (SNR~3), as attested by the reduced precision of the corresponding thermometry (5.4%).

4.3. Relative O_2/CO_2 concentration measurements

The relative O_2/CO_2 concentrations in the flue gases of the hydrocarbon flame can be measured by comparing the spectral signatures of the O_2 and CO_2 molecules in the experimental CSRS spectra. A contour-fitting routine is employed to compare the experimental ro-vibrational O_2-CO_2 spectra to a library of synthetic spectra, computed for relative O_2/CO_2 concentrations ranging from 0 to 4, in steps of 0.1. As mentioned in the previous paragraph, in the flame experiment the O_2 spectrum is only detected with a reasonable SNR up to φ=0.84, so that the relative O_2/CO_2 concentrations can be measured for four lean flame conditions. Table 2 summarises the experimental relative O_2/CO_2 concentrations measured from the ro-vibrational Raman spectra, at the different flame conditions. As expected, the relative oxygen content in the product of the premixed laminar flame is reduced for increasing values of the equivalence ratio up to 0.84: for the richer flame conditions tested (φ=0.93, 1.05) the ro-vibrational O_2 spectrum was, respectively, too weak to perform quantitative measurements on it and not detected altogether. When compared to the expected relative concentrations, the experimental measurements result in a significant overestimation of the oxygen content relative to carbon dioxide.

One of the possible reasons for this measurement bias is identified in the spectral referencing of the ro-vibrational O_2-CO_2 spectra, performed by subdividing the experimental resonant spectra by the spectrum of the NR CSRS signal, generated in a gas with no ro-vibrational degree of freedom (i.e. argon), which maps the excitation efficiency at different Raman shifts. As it propagates through different optical media, the ultrabroadband pump/Stokes pulse can be affected by changes in the group velocity dispersion [75], resulting in temporal chirp, which limits the bandwidth effective excitation efficiency at the measurement location [76–80]. In addition, the self-phase modulation experienced by the pulse during the pulse propagation in the filament –being a third-order nonlinear optical process– depends on the composition and temperature of the gas-phase medium. It is, therefore, possible that the NR CSRS signal acquired *ex-situ*, in argon, does not perfectly map the ultrabroadband excitation efficiency, when this is generated *in-situ*. This would have a negligible effect on ro-vibrational thermometry, as the ro-vibrational O_2 and the "blue" CO_2 Q-branch spectra span less than 60 cm^{-1} at high temperatures. An imperfect spectral referencing, on the other hand, could significantly affect the relative intensity of the ro-vibrational spectra of the two species and, thus, the relative O_2/CO_2 concentration measurements.

5. Conclusions and outlook

We have demonstrated ultrabroadband two-beam fs/ps coherent Raman spectroscopy for simultaneous O_2-CO_2 thermometry and relative concentration measurements, employing fs-laser-induced filamentation for the supercontinuum generation. The 35 fs duration output of a regenerative Ti:Sapphire amplifier system, with 1.6 mJ/pulse, is focused to the measurement location so as to induce Kerr effect in the gas-phase medium resulting in the beam self-focusing and the generation of a plasma filament. While travelling inside this filament the pulse experiences self-phase modulation and temporal compression resulting in the generation of a compressed supercontinuum. The pulse energy conversion efficiency in the filamentation process is constant over the whole

range of input pulse energy measured, and it only slightly depends on the temperature and composition of the gas-phase medium: in the hot products of a CH_4/air flame the conversion efficiency was measured to be ~86%, as compared to the ~82% efficiency measured in air. The resulting ~24 fs duration output of the filament is thus employed as the pump/Stokes pulse in a two-beam fs/ps CARS setup: the bandwidth of the pulse is sufficient to impulsively excite the ro-vibrational coherences of the Raman-active molecules up to 1600 cm^{-1}. The use of the fs-laser-induced filament as the supercontinuum source thus allows for the practical implementation of ultrabroadband coherent Raman spectroscopy with a single regenerative laser amplifier. Furthermore, the *in-situ* generation and *in-situ* use of the filament can pave the way to the application of ultrabroadband CARS spectroscopy in combustion scenarios where the pulse needs to be transmitted through thick optical windows, which severely limit the effective excitation bandwidth delivered by broadband pulses generated *ex-situ* [81]. The demonstration of coherent Raman spectroscopy with ultrabroadband femtosecond laser excitation generated *in-situ* behind thick optical ports, and the characterization of its performance for thermometry and relative species concentration measurements represents the next step in our research on this topic.

A time-domain model for the ro-vibrational O_2 and CO_2 CSRS signal has been developed, in order to fit the experimental spectra and extract temperatures and relative O_2/CO_2 concentrations. The time-domain modelling of the CO_2 spectrum, in particular, employs recently available comprehensive calculations of the polarizability transition moments for Raman transitions in the range 1150–1500 cm^{-1} [57]. The availability of these data allows for up to 180 vibrational bands to be included in the time-domain simulation of the CSRS signal. In order to validate this spectral model, and demonstrate simultaneous ro-vibrational thermometry and relative concentration measurements on the ro-vibrational O_2 and CO_2 spectra, filament-based ultrabroadband coherent Raman spectroscopy was successfully employed in the product gases of a laminar premixed methane/air flame. The flame measurements are performed on a Bunsen burner, at six different values of the equivalence ratio, from 0.6 to 1.05. The experimental spectra are acquired on the Stokes side (CSRS), rather than on the anti-Stokes one (CARS), owing to the larger excitation efficiency provided on the Stokes side by the ultrabroadband pump/Stokes pulse generated *in-situ*. Single-shot detection of the ro-vibrational O_2 and CO_2 spectra is demonstrated in all of the flame conditions tested; nevertheless, the signal rapidly degrades with the temperature increment, significantly reducing the single-to-noise-ratio. This fact limits the applicability of the proposed diagnostic technique to high temperatures: such a limitation could be overcome by increasing the energy content of the probe pulse or by employing a separate high-power ps laser source. In addition, the signal detection could be improved by employing a more sensitive CCD detector, instead of the sCMOS one currently in use in our set-up. In order to guarantee a sufficient SNR to validate the spectral model at temperatures higher than 2000 K, in the present work, the CSRS spectra acquired in the flame are therefore averaged over 40 laser-shots.

The ro-vibrational temperature is independently measured by fitting the ro-vibrational spectra of the two species –ranging 1480–1560 cm^{-1} for O_2 and 1375–1450 cm^{-1} for the CO_2 "blue" dyad– to distinct spectral libraries: the experimental results show a good agreement between O_2 and CO_2 thermometry. The measured temperatures are moreover validated by comparison to the adiabatic flame temperature and by performing pure-rotational N_2-O_2 CARS thermometry at the same flame conditions: ro-vibrational CO_2 thermometry presents an accuracy of −5.3% and a precision of 0.7% at 2200 K. The relatively complex vibrational energy structure of the CO_2 molecule results in the high temperature sensitivity of its ro-vibrational Raman spectrum. In this respect, possible refinements of the position and strength of its ro-vibrational spectral lines could further improve CO_2 vibrational thermometry at temperatures higher than 2000 K. Simultaneously to thermometry, relative O_2/CO_2 concentration measurements are performed by comparing the relative intensity of the ro-vibrational spectra of the two species. When employed to measure the relative concentrations in the flame products, this technique results in a significant overestimation of the oxygen content, relative to carbon dioxide. We speculate that this mismatch can be attributed, at least in part, to the *ex-situ* spectral referencing of the ultrabroadband femtosecond laser excitation generated *in-situ*.

In conclusion, the present work represents a further step towards quantitative ultrabroadband fs/ps coherent Raman spectroscopy in the molecular fingerprint region, for simultaneous thermometry and relative concentration measurements in chemically-reacting flows. We are currently pursuing the development and validation of time-domain models of the ro-vibrational Raman spectra of major species for combustion diagnostics, such as CH_4 [82] and H_2.

Declaration of Competing Interest

The authors declare that they have no known competing financial interests or personal relationships that could have appeared to influence the work reported in this paper.

Acknowledgments

We gratefully acknowledge the financial support provided by the Netherlands Organization for Scientific Research (NWO), obtained through a Vidi grant in the Applied and Engineering Sciences domain (AES) (15690). In addition, A. Bohlin is thankful for support through the RIT project/European Regional Development Fond. We thank Dr. Michele Marrocco for his valuable comments on the application of the time-domain CARS model to CSRS spectra, and M.Sc. thesis student Aert Stutvoet for technical assistance in the experiments.

Supplementary materials

Supplementary material associated with this article can be found, in the online version, at doi:10.1016/j.combustflame.2021.111738.

References

[1] J.B. Zheng, A. Leipertz, J.B. Snow, R.K. Chang, Simultaneous observation of rotational coherent Stokes Raman scattering and coherent anti-Stokes Raman scattering in air and nitrogen, Opt. Lett. 8 (7) (1983) 350–352.
[2] A.C. Eckbreth, T.J. Anderson, Simultaneous rotational coherent anti-Stokes Raman spectroscopy and coherent Stokes Raman spectroscopy with arbitrary pump-Stokes spectral separation, Opt. Lett. 11 (8) (1986) 496–498.
[3] A.C. Eckbreth, Laser Diagnostics For Combustion Temperature and Species, Second Edi, Gordon and Breach Publishers, 1996.
[4] W.R. Lempert, I.V. Adamovich, Coherent anti-Stokes Raman scattering and spontaneous Raman scattering diagnostics of nonequilibrium plasmas and flows, J. Phys. D. Appl. Phys. 47 (2014) 433001.
[5] F. Moya, S.A.J. Druet, J.P.E. Taran, Gas spectroscopy and temperature measurement by coherent Raman anti-stokes scattering, Opt. Commun. 13 (2) (1975) 169–174.
[6] A.C. Eckbreth, CARS thermometry in practical combustors, Combust. Flame 39 (2) (1980) 133–147.
[7] T. Seeger, A. Leipertz, Experimental comparison of single-shot broadband vibrational and dual-broadband pure rotational coherent anti-Stokes Raman scattering in hot air, Appl. Opt. 35 (15) (1996) 2665–2671.
[8] P.R. Régnier, J.P.E. Taran, On the possibility of measuring gas concentrations by stimulated anti-Stokes scattering, Appl. Phys. Lett. 23 (5) (1973) 240–242.
[9] P.R. Régnier, F. Moya, J.P.E. Taran, Gas concentration measurement by coherent raman anti-stokes scattering, AIAA J. 12 (6) (1974) 826–831.
[10] S. Roy, J.R. Gord, A.K. Patnaik, Recent advances in coherent anti-Stokes Raman scattering spectroscopy: fundamental developments and applications in reacting flows, Prog. Energy Combust. Sci. 36 (2) (2010) 280–306.

[11] A. Bohlin, B.D. Patterson, C.J. Kliewer, Communication: simplified two-beam rotational CARS signal generation demonstrated in 1D, J. Chem. Phys. 138 (2013) 081102.
[12] M. Scherman, et al., 1-kHz hybrid femtosecond/picosecond coherent anti-Stokes Raman scattering thermometry of turbulent combustion in a representative aeronautical test rig, J. Raman Spectrosc (2021) In press.
[13] S. Legros, et al., Combustion for aircraft propulsion: progress in advanced laser-based diagnostics on high-pressure kerosene/air flames produced with low-NOx fuel injection systems, Combust. Flame 224 (2021) 273–294.
[14] R.W. Boyd, Nonlinear Optics, 3rd Ed., Academic Press Inc., 2013.
[15] D.A. Long, The Raman effect: A unified Treatment of the Theory of Raman scattering By Molecules, 1st Ed., John Wiley & Sons Ltd., 2002.
[16] L. Castellanos, F. Mazza, D. Kliukin, A. Bohlin, Pure-rotational 1D-CARS spatiotemporal thermometry with a single regenerative amplifier system, Opt. Lett. 45 (17) (2020) 4662–4665.
[17] P. Polynkin, Y. Chen, Air Lasing, 1st ed., Springer International Publishing, 2018.
[18] S. Roy, P. Wrzesinski, D. Pestov, T. Gunaratne, M. Dantus, J.R. Gord, Single-beam coherent anti-Stokes Raman scattering spectroscopy of using a shaped 7 fs laser pulse, Appl. Phys. Lett. 95 (2009) 074102.
[19] A. Bohlin, C.J. Kliewer, Two-beam ultrabroadband coherent anti-Stokes Raman spectroscopy for high resolution gas-phase multiplex imaging, Appl. Phys. Lett. 104 (2014) 031107.
[20] A. Bohlin, C.J. Kliewer, Direct Coherent Raman Temperature Imaging and Wideband Chemical Detection in a Hydrocarbon Flat Flame, J. Phys. Chem. Lett. 6 (2015) 643–649.
[21] A. Bohlin, C. Jainski, B.D. Patterson, A. Dreizler, C.J. Kliewer, Multiparameter spatio-thermochemical probing of flame-wall interactions advanced with coherent Raman imaging, Proc. Combust. Inst. 36 (3) (2017) 4557–4564.
[22] J.H. Odhner, D.A. Romanov, R.J. Levis, Rovibrational wave-packet dispersion during femtosecond laser filamentation in air, Phys. Rev. Lett. 103 (2009) 075005.
[23] G. Rouillé, G. Millot, R. Saint-Loup, H. Berger, High-resolution stimulated Raman spectroscopy of O_2, J. Mol. Spectrosc. 154 (1992) 372–382.
[24] B. Lavorel, et al., Study of collisional effects on band shapes of the $\nu_1/2\nu_2$ Fermi dyad in CO_2 gas with stimulated Raman spectroscopy. I. Rotational and vibrational relaxation in the $2\nu_2$ band, J. Chem. Phys. 174 (1994) 2176–2184 1998.
[25] T.L. Courtney, A. Bohlin, B.D. Patterson, C.J. Kliewer, Pure-rotational H_2 thermometry by ultrabroadband coherent anti-stokes Raman spectroscopy, J. Chem. Phys. 146 (2017) 224202.
[26] G. Magnotti, U. KC, P.L. Varghese, R.S. Barlow, Raman spectra of methane, ethylene, ethane, dimethyl ether, formaldehyde and propane for combustion applications, J. Quant. Spectrosc. Radiat. Transf. 163 (2015) 80–101.
[27] A. Cavaliere, M. De Joannon, Mild combustion, Prog. Energy Combust. Sci. 30 (2004) 329–366.
[28] D. Tabacco, C. Innarella, C. Bruno, Theoretical and numerical investigation in flameless combustion, Combust. Sci. Technol. 174 (7) (2002) 1–35.
[29] A.A.V. Perpignan, A.Gangoli Rao, D.J.E.M. Roekaerts, Flameless combustion and its potential towards gas turbines, Prog. Energy Combust. Sci. 69 (2018) 28–62.
[30] J.W. Tröger, C. Meißner, T. Seeger, High temperature O_2 vibrational CARS thermometry applied to a turbulent oxy-fuel combustion process, J. Raman Spectrosc. 47 (2016) 1149–1156.
[31] R.J. Hall, J.H. Stufflebeam, Quantitative CARS spectroscopy of CO_2 and N_2O, Appl. Opt. 23 (23) (1984) 4319–4327.
[32] R.P. Lucht, et al., Dual-pump coherent anti-stokes Raman scattering temperature and CO_2 concentration measurements, AIAA J. 41 (4) (2003) 679–686.
[33] S. Roy, T.R. Meyer, R.P. Lucht, V.M. Belovich, E. Corporan, J.R. Gord, Temperature and CO_2 concentration measurements in the exhaust stream of a liquid-fueled combustor using dual-pump coherent anti-Stokes Raman scattering (CARS) spectroscopy, Combust. Flame 138 (3) (2004) 273–284.
[34] M. Kerstan, I. Makos, S. Nolte, A. Tünnermann, R. Ackermann, Two-beam femtosecond coherent anti-Stokes Raman scattering for thermometry, Appl. Phys. Lett. 110 (2017) 021116.
[35] Y. Ran, M. Junghanns, A. Boden, S. Nolte, A. Tünnermann, R. Ackermann, Temperature and gas concentration measurements with vibrational ultra-broadband two-beam femtosecond/picosecond coherent anti-Stokes Raman scattering and spontaneous Raman scattering, J. Raman Spectrosc. 50 (2019) 1268–1275.
[36] R.P. Lucht, R.E. Palmer, M.A. Maris, Simultaneous acquisition of pure rotational and vibrational nitrogen spectra using three-laser coherent anti-Stokes Raman spectroscopy, Opt. Lett. 12 (6) (1987) 386–388.
[37] F. Vestin, M. Afzelius, P.E. Bengtsson, Development of rotational CARS for combustion diagnostics using a polarization approach, Proc. Combust. Inst. 31 (1) (2007) 833–840.
[38] A. Bohlin, M. Mann, B.D. Patterson, A. Dreizler, C.J. Kliewer, Development of two-beam femtosecond/picosecond one-dimensional rotational coherent anti-Stokes Raman spectroscopy: time-resolved probing of flame wall interactions, Proc. Combust. Inst 35 (3) (2015) 3723–3730.
[39] S.L. Chin, *Femtosecond Laser Filamentation*, First Edit, Springer, New York, NY, 2010.
[40] A. Mysyrowicz, A. Couairon, U. Keller, Self-compression of optical laser pulses by filamentation, New J. Phys. 10 (2008) 025023.
[41] A. Couairon, M. Franco, G. Méchain, T. Olivier, B. Prade, A. Mysyrowicz, Femtosecond filamentation in air at low pressures: part I: theory and numerical simulations, Opt. Commun. 259 (2006) 265–273.
[42] A. Couairon, et al., Self-compression of ultra-short laser pulses down to one optical cycle by filamentation, J. Mod. Opt. 53 (1–2) (2006) 75–85.
[43] M.A. Yuratich, Effects of laser linewidth on coherent antiStokes Raman spectroscopy, Mol. Phys. 38 (2) (1979) 625–655.
[44] H.U. Stauffer, et al., Time- and frequency-dependent model of time-resolved coherent anti-Stokes Raman scattering (CARS) with a picosecond-duration probe pulse, J. Chem. Phys. 140 (2014) 024316.
[45] Y. Liu, P. Ding, G. Lambert, A. Houard, V. Tikhonchuk, A. Mysyrowicz, Recollision-Induced Superradiance of Ionized Nitrogen Molecules, Phys. Rev. Lett. 115 (2015) 133203.
[46] Z. Liu, et al., Extremely nonlinear Raman interaction of an ultrashort nitrogen ion laser with an impulsively excited molecular wave packet, Phys. Rev. A 101 (2020) 043404.
[47] B.D. Prince, et al., Development of simultaneous frequency- and time-resolved coherent anti-Stokes Raman scattering for ultrafast detection of molecular Raman spectra, J. Chem. Phys 125 (2006) 044502.
[48] J.D. Miller, S. Roy, M.N. Slipchenko, J.R. Gord, T. Meyer, Single-shot gas-phase thermometry using pure-rotational hybrid femtosecond/picosecond coherent anti-Stokes Raman scattering, Opt. Express 19 (16) (2011) 15627–15640.
[49] S.P. Kearney, D.J. Scoglietti, C.J. Kliewer, Hybrid femtosecond/picosecond rotational coherent anti-Stokes Raman scattering temperature and concentration measurements using two different picosecond-duration probes, Opt. Express 21 (10) (2013) 12327–12339.
[50] T.Y. Chen, C.J. Kliewer, B.M. Goldberg, E. Kolemen, Y. Ju, Time-domain modelling and thermometry of the CH_4 ν_1 Q-branch using hybrid femtosecond/picosecond coherent anti-Stokes Raman scattering, Combust. Flame 224 (2021) 183–195.
[51] K. Bito, M. Okuno, H. Kano, P. Leproux, V. Couderc, H. Hamaguchi, Three-pulse multiplex coherent anti-Stokes/Stokes Raman scattering (CARS/CSRS) microspectroscopy using a white-light laser source, Chem. Phys. 419 (2013) 156–162.
[52] P.V. Kolesnichenko, J.O. Tollerud, J.A. Davis, Background-free time-resolved coherent Raman spectroscopy (CSRS and CARS): heterodyne detection of low-energy vibrations and identification of excited-state contributions, APL Photonics 4 (2019) 056102.
[53] G. Herzberg, Molecular Spectra and Molecular Structure, II. Infrared and Raman Spectra of Polyatomic Molecules, First Edit. D. Van Nostrand Company Inc, 1945.
[54] P.F. Bernath, *Spectra of Atoms and Molecules*, Second Edi, Oxford University Press Inc., 2005.
[55] M. Basire, et al., Fermi resonance in CO_2: mode assignment and quantum nuclear effects from first principles molecular dynamics, J. Chem. Phys. 146 (2017) 134102.
[56] L.S. Rothman, R.L. Hawkins, R.B. Wattson, R.R. Gamache, Energy levels, intensities, and linewidths of atmospheric carbon dioxide bands, J. Quant. Spectrosc. Radiat. Transf 48 (5–6) (1992) 537–566.
[57] R. Lemus, M. Sánchez-Castellanos, F. Pérez-Bernal, J.M. Fernández, M. Carvajal, Simulation of the Raman spectra of CO_2: bridging the gap between algebraic models and experimental spectra, J. Chem. Phys 141 (2014) 054306.
[58] G. Tejeda, B. Maté, S. Montero, Overtone Raman spectrum and molecular polarizability surface of CO_2, J. Chem. Phys. 103 (2) (1995) 568–576.
[59] M. Gu, A. Satija, R.P. Lucht, CO_2 chirped-probe-pulse femtosecond CARS thermometry, Proc. Combust. Inst. 38 (1) (2021) 1599–1606.
[60] C.M. Penney, L.M. Goldman, M. Lapp, Raman Scattering Cross Sections, Nat. Phys. Sci. 235 (1972) 110–112.
[61] L.A. Rahn, R.E. Palmer, Studies of nitrogen self-broadening at high temperature with inverse Raman spectroscopy, J. Opt. Soc. Am. B 3 (9) (1986) 1164–1169.
[62] L. Rosenmann, J.M. Hartmann, M.Y. Perrin, J. Taine, Accurate calculated tabulations of IR and Raman CO_2 line broadening by CO_2, H_2O, N_2, O_2 in the 300-2400-K temperature range, Appl. Opt 27 (18) (1988) 3902–3907.
[63] V.G. Arakcheev, et al., Collisionally induced dephasing and rotational energy transfer in the CO_2 Fermi dyad 'red' Q-branch 1285 cm^{-1}, J. Raman Spectrosc. 38 (2007) 1038–1045.
[64] V.G. Arakcheev, et al., Collisionally induced dephasing and rotational energy transfer in the CO_2 Fermi dyad 'blue' Q-branch 1388 cm^{-1}, J. Raman Spectrosc. 38 (2007) 1046–1051.
[65] L. Martinsson, P.-.E. Bengtsson, M. Aldén, Oxygen concentration and temperature measurements in N_2-O_2 mixtures using rotational coherent anti-Stokes Raman spectroscopy, Appl. Phys. B Lasers Opt. 62 (1996) 29–37.
[66] J.I. Hölzer, C. Meißner, T. Seeger, Oxygen rotational Raman linewidth determination considering nonmonoexponential decoherence behavior, J. Raman Spectrosc. 50 (2019) 1260–1267.
[67] T.L. Courtney, C.J. Kliewer, Rotational coherence beating in molecular oxygen: coupling between electronic spin and nuclear angular momenta, J. Chem. Phys. 149 (2018) 234201.
[68] M.A. Buldakov, V.N. Cherepanov, B.V. Korolev, I.I. Matrosov, Role of intramolecular interactions in Raman spectra of N_2 and O_2 molecules, J. Mol. Spectrosc. 217 (1) (2003) 1–8.
[69] G. Millot, R. Saint-Loup, J. Santos, R. Chaux, H. Berger, J. Bonamy, Collisional effects in the stimulated Raman Q-branch of O_2 and O_2-N_2," J, Chem. Phys 96 (2) (2011) 961–971.
[70] A.E. DePristo, S.D. Augustin, R. Ramaswamy, H. Rabitz, Quantum number and energy scaling for nonreactive collisions, J. Chem. Phys. 71 (2) (1979) 850–865.
[71] D.K. Veirs, G.M. Rosenblatt, Raman line positions in molecular hydrogen: H_2, HD, HT, D_2, DT, and T_2„ J. Mol. Spectrosc. 121 (2) (1987) 401–419.

[72] J.A. van Oijen, L.P.H. de Goey, Modelling of premixed laminar flames using flamelet-generated manifolds, Combust. Sci. Technol. 161 (1) (2000) 113–137.
[73] S.P. Kearney, Hybrid fs/ps rotational CARS temperature and oxygen measurements in the product gases of canonical flat flames, Combust. Flame 162 (5) (2014) 1748–1758.
[74] D.R. Richardson, H.U. Stauffer, S. Roy, J.R. Gord, Comparison of chirped-probe-pulse and hybrid femtosecond/picosecond coherent anti-Stokes Raman scattering for combustion thermometry, Appl. Opt. 56 (11) (2017) 37–49.
[75] P.J. Wrzesinski, D. Pestov, V.V. Lozovoy, J.R. Gord, S. Roy, Group-velocity-dispersion measurements of atmospheric and combustion-related gases using an ultrabroadband-laser source, Opt. Express 19 (6) (2011) 8394–8401.
[76] M. Gu, A. Satija, R.P. Lucht, Impact of moderate pump/Stokes chirp on femtosecond coherent anti-Stokes Raman scattering spectra, J. Raman Spectrosc. 51 (2020) 115–124.
[77] F. Mazza, L. Castellanos, D. Kliukin, A. Bohlin, Coherent Raman imaging thermometry with *in-situ* referencing of the impulsive excitation efficiency, Proc. Combust. Inst 38 (1) (2021) 1895–1904.
[78] J.-.L. Oudar, Y.R. Shen, Nonlinear spectroscopy by multiresonant four-wave mixing, Phys. Rev. A 22 (3) (1980) 1141–1158.
[79] R.L. Farrow, P.L. Mattern, L.A. Rahn, Comparison between CARS and corrected thermocouple temperature measurements in a diffusion flame, Appl. Opt. 21 (17) (1982) 3119–3125.
[80] R.L. Farrow, R.P. Lucht, G.L. Clark, R.E. Palmer, Species concentration measurements using CARS with nonresonant susceptibility normalization, Appl. Opt 24 (14) (1985) 2241–2251.
[81] S.P. Kearney, Bandwidth optimization of femtosecond pure-rotational coherent anti-Stokes Raman scattering by pump/Stokes spectral focusing, Appl. Opt 53 (28) (2014) 6579–6585.
[82] T.D. Butterworth, B. Amyay, T. Minea, N. Gatti, Q. Ong, Quantifying methane vibrational and rotational temperature with Raman scattering, J. Quant. Spectrosc. Radiat. Transf 236 (2019) 106562.